Calibration of programmable spectral imager with dual disperser architecture

Elizabeth Hemsley, Simon Lacroix, Hervé Carfantan, Antoine Monmayrant

Calibration of Programmable Spectral Imager with Dual Disperser Architecture

Elizabeth Hemsley[a,*], Simon Lacroix[a], Hervé Carfantan[b], Antoine Monmayrant[a]

[a] *LAAS-CNRS, Université de Toulouse, CNRS, 7 Avenue du Colonel Roche, 31400 Toulouse, France*
[b] *IRAP, Université de Toulouse, CNRS, CNES, 14 Avenue Édouard Belin, 31400 Toulouse, France*

Abstract

We present a hyperspectral imager with a dual disperser architecture, which is highly re-configurable thanks to the use of a digital micro-mirror device (DMD). The system has over 200 spectral bands in the range 400 - 700 nm, and 2048 by 2048 spatial pixels. We describe a method to calibrate the instrument and quantify its performance using a simple slit scanning acquisition scheme, and discuss various methods to remove artifacts in the spectral datacube via post-processing. This prototype instrument is designed for simplicity, and aims to explore new acquisition schemes that exploit the property of colocation and use the programmable nature of the DMD to increase the speed of datacube retrieval and the quality of the hyperspectral data.

1. Introduction

Hyperspectral imaging is a form of spectroscopy whereby spectral information is found for each location in a 2D scene, and has proved useful for numerous applications, including remote sensing, earth observation, medical imaging, food inspection. There are many different types of hyperspectral imagers, [1, 2, 3], but all require that the 3D hyperspectral information, known as the datacube, is measured on a detector array with 1 or 2 dimensions. Without making any assumptions on the sparsity or redundancy of the data, obtaining the datacube requires multiple acquisitions in space or time, and in addition to improving the design of the instrument itself, it is important to develop efficient acquisition algorithms to optimize frame rate, resolution, and SNR.

The use of digital micro-mirror devices (DMDs) in hyperspectral imagers has become more commonplace in recent years, for various architectures [4, 5, 6, 7]. DMDs provide highly re-configurable spatial filtering with no moving parts,

*Corresponding author
Email address: elizabeth.hemsley@laas.fr (Elizabeth Hemsley)

and compared to other spatial light modulators, they are fast, efficient and have neither polarization nor wavelength dependency. A hyperspectral imager based on a dual-disperser architecture can make effective use of DMD technology. This particular architecture differs from other configurations mainly due to the property of colocation; each point on the scene corresponds exactly to a point on the detector array, with the DMD applying spatio-spectral filtering. There is no spatio-spectral coupling on the image recorded by the camera, and when all the mirrors on the DMD are turned to the 'on' position, the panchromatic image is registered on the camera.

A broad range of acquisition schemes may be implemented using dual disperser systems. For example, one can perform Hadamard transform spectroscopy by applying a Hadamard mask on the DMD, improving SNR via the Fellgett advantage [8, 9, 10, 11, 12]. By making adjustments to the system (using a telecentric lens system), it is possible to perform near-snapshot spectral filtering [13, 8, 14, 15, 16], identifying target chemicals with a fast frame rate. There is also interest in reducing the number of acquisitions required per datacube; recent work has measured the spectrum using a Fourier basis, which can reduce the number of acquisitions, as long as there are no sharp spectral features [17]. Classification of multiple spectra is possible with only a few acquisitions as shown in [18, 19], using a scheme where the DMD mask adapts for each new acquisition to improve classification accuracy. Furthermore, there is potential to use regularization approaches to exploit homogeneity within the hyperspectral datacube, allowing full cube reconstruction with only a handful of acquisitions [20]. The easy access to the panchromatic image allows an adaptive approach to datacube acquisition, whereby one exploits features from the panchromatic image to optimize the DMD mask for a particular acquisition scheme, or even change the acquisition scheme itself. As such there are likely many other acquisition schemes that can be developed using this architecture, leveraging the property of colocation and the easy access to the panchromatic image to develop highly adaptable, fast, and re-configurable schemes.

However, with all this potential, there is little discussion in the literature of the basic optical properties and the calibration of the system, or of common issues with the data acquired by such device. In this work therefore we hope to remedy this by providing a comprehensive explanation of the system itself; the layout, underlying optical equations, and method of calibration, demonstrating these methods on a prototype device. This work aims to lay the foundation to develop more sophisticated acquisition schemes in the future.

Section 2 describes the key principles and optical layout of our prototype dual-disperser type hyperspectral imager, and section 3 outlines the theoretical model and procedure to calibrate the device, and discusses the influence of distortion. In section 4 we test the device using a simple slit-scanning acquisition scheme with a variable slit width, and describe how to reconstruct the hyperspectral datacube. We note the presence of periodic artifacts in the datacube, arising from the use of the DMD, and so in Section 5 we present three approaches to correct these artifacts and improve accuracy of the spectral measurements. Section 6 discusses the final results, and aims to benchmark the

system, allowing a comparison to other acquisition schemes. Section 7 concludes the paper.

2. System overview

2.1. Principle

A dual-disperser type hyperspectral imager re-images the scene twice, first on the DMD, which applies programmable spatio-spectral filtering, and finally on the camera. The basic optical layout of the system is shown in Figure 1, comprising of a two 4-f imaging systems back to back, with a prism operating as the dispersive element in the middle of each 4-f line. A beam splitter (BS) is used to image the filtered scene onto a camera.

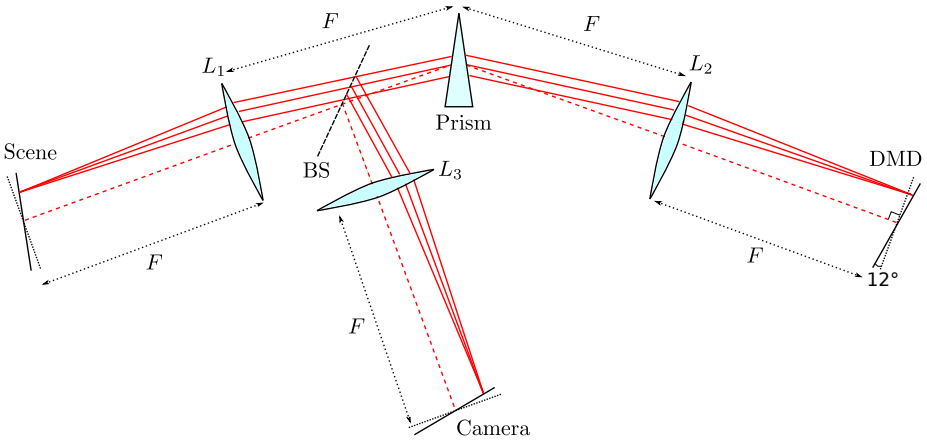

Figure 1: Schematic of system layout, showing tilting of scene and camera to compensate the angle of DMD to optical axis

We use a prism as the dispersive component. Hyperspectral imagers often use gratings due to their roughly linear dispersion and lack of distortion, however high efficiency gratings are typically very dispersive, and for systems with long focal lengths (as in our case) or large spectral bandwidths it is challenging to find a suitable grating; the spatial extent of the spectrum is wider than the DMD, or there is overlap between first and higher orders. Conversely, prisms are suitable for a wide range of system sizes and bandwidths, and as we demonstrate in Section 3, optical distortion is easily compensated, as long as the system has a small enough field of view. Additionally, if the system is operating in a low flux environment, a prism typically has a much higher and uniform transmission efficiency, independent from polarization, and unlike a grating does not suffer from stray light originating from higher diffraction orders.

2.2. Co-location property

At the camera, the image has the property of colocation; each 'pixel' on the scene corresponds exactly to a pixel on the camera, with no wavelength

dependent spatial transformation. If all the micro-mirrors on the DMD are turned to the 'on' position, i.e. reflecting light to the camera, the panchromatic image is obtained on the camera.

At the DMD, the image is spectrally dispersed such that the location of the image on the DMD depends on the wavelength. When a mask is applied to the DMD, each wavelength from the scene is spatially filtered by a laterally shifted copy of the DMD mask. In other words, the spectral filtering applied by the DMD depends on the location of the scene pixel, as illustrated in Figure 2 – and demonstrated in section 3.1. As the spectrum is dispersed in one direction on the DMD, each horizontal line of the scene is independent, and can be individually addressed by the DMD.

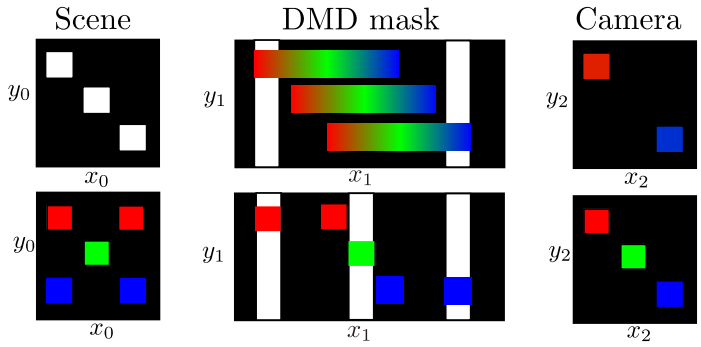

Figure 2: Schematic illustrating colocation between scene and camera, with spatially dependent spectral filtering applied by the DMD mask.

2.3. Prototype specifications

A photograph of the system is shown in Figure 3. In our case the layout is folded along the optical path by reflection from the DMD. The folded system is compact and easy to align, but requires a beamsplitter to direct the reflected light to the camera, resulting in a 75% loss of flux. As this system is a prototype device, concerned with developing novel acquisition methods, the system efficiency itself is not an essential metric. If one is concerned with transmission efficiency, or operates in a low flux environments (for example satellite imaging), it is fairly trivial to unfold the optical path, at the cost of a larger and more complex setup.

The system is designed for visible light in the range 400-700 nm, and uses Thorlab lenses TL200 with focal length 200 mm, and numerical aperture 0.05. The prism is a custom BK7 prism with apex angle 30° and AR coating. The DMD is part of the DLP Discovery 4100 Development Kit, which has an array of 1920 by 1080 individual square mirrors with period 10.8 μm. Each mirror rotates along its diagonal axis by $\pm 12°$. For simplicity in aligning and building the system on a horizontal plane on a typical optical table, the DMD is rotated by 45°, so the diagonal axis of each mirror is vertical, avoiding cumbersome 3D geometries. Unlike a normal mirror, the plane of the DMD must be tilted at 12°

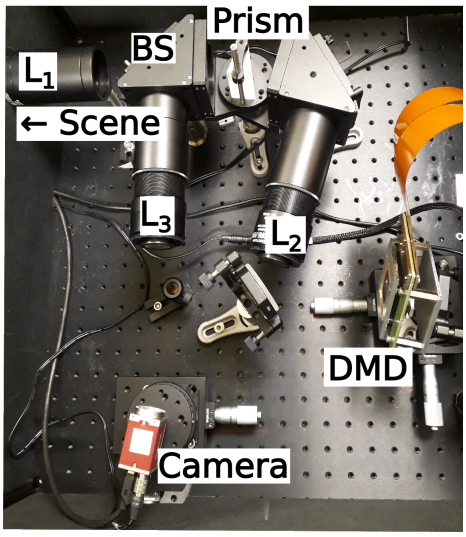

Figure 3: System prototype

relative to the optical axis in the horizontal plane, and therefore the object and image planes are also tilted to compensate, fulfilling the Scheimpflug condition [21]. The maximum switching rate for the DMD is 23,148 Hz.

The camera is CMOS Mako model G419B, which has 2048 by 2048 square pixels with pitch 5.5 μm, giving an angular field of view of 3.22°. The maximum frame rate of this camera is 26.3 fps, and bit depth of 12. The camera pixel is significantly smaller than the DMD mirror, which means that in addition to the 45° rotation of the DMD, we do not have a 1 to 1 relationship between camera pixel and DMD mirror. The ramifications of this mismatch are discussed further in Section 4.

The imaging properties of the device were measured using standard procedures (see Appendix A). There was no distortion found in the resulting camera image, and the spatial resolution is approximately 11 μm, or 2 pixels. The point spread function (PSF) was found largely independent of the wavelength and fairly constant across the field of view.

3. Calibration

In this section we begin by explaining the relationship between the DMD and the camera using simple ray optics, resulting a function which maps a location on the camera to a particular DMD pixel, dependent on wavelength. We then describe the calibration procedure which determines the key parameters of this function, and discuss the accuracy of the model. We also address the influence of smile distortion, and demonstrate how to compensate this effect in the calibration functions.

3.1. Theory

The dual disperser hyperspectral imager has three focal planes; defined by coordinates (x_0, y_0) at the scene, (x_1, y_1) at the DMD, and (x_2, y_2) at the camera (see Figure 4). As this system is line independent in the y direction [22], we begin by concentrating on the case where $y_0 = y_1 = y_2 = 0$, i.e. a horizontal cross-section through the system. A schematic of the unfolded optical system is shown in Figure 4.

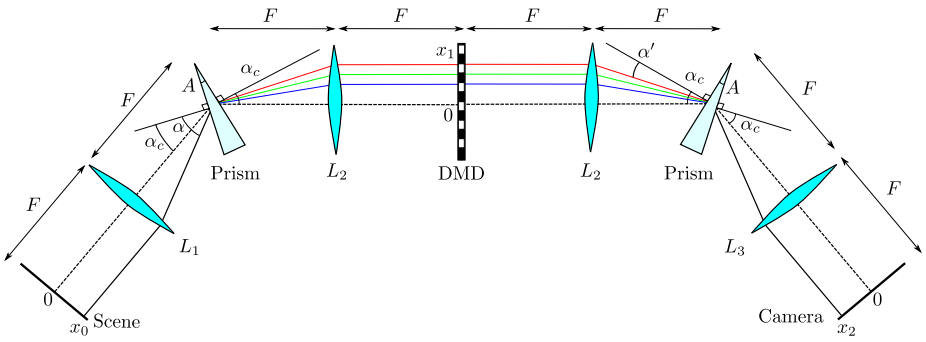

Figure 4: Schematic of dual disperser hyperspectral imager. Dashed line denotes the optical axis.

The central wavelength, $\lambda_c = 550\,\text{nm}$, is aligned along the optical axis, which corresponds to the angle of minimum deviation at the prism. The symmetry of the system leads to colocation between the scene and the camera, i.e. $(x_0, y_0) = (x_2, y_2)$, but due to dispersion via the prism, the ray incident on the DMD is laterally shifted in x_1 dependent on the wavelength, apart from λ_c where we have $x_0 = x_1 = x_2$.

The angle of deviation of a prism is given by

$$\theta_D(\lambda, \alpha) = \alpha - A + \arcsin\left(n(\lambda)\sin\left(A - \arcsin\left[\frac{\sin(\alpha)}{n(\lambda)}\right]\right)\right) \tag{1}$$

Where α is the angle of incidence, A is the apex angle of the prism and $n(\lambda)$ the refractive index. The mapping between a location at the scene and a point on the DMD, for focal length F, is given by

$$x_1(\lambda, x_0) = F\tan\left(\theta_D\left(\lambda, \alpha(x_0)\right) - \alpha(x_0) + A - \alpha_c\right) \tag{2}$$

The reference angle of incidence α_c gives the angle of minimum deviation for the wavelength λ_c, and is the angle between the optical axis to the prism:

$$\alpha_c = \arcsin\left(n(\lambda_c)\sin(A/2)\right) \tag{3}$$

Note that here we have ignored the influence of the 12° tilt between the normal to the focal planes and the optical axis, as its influence is negligible. The angle of incidence at the prism depends on the scene location x_0, given by

$$\alpha(x_0) = \alpha_c + \arctan\left(\frac{x_0}{F}\right) \tag{4}$$

Substituting Equations (4) and (1) into (2) gives

$$x_1(\lambda, x_0) = F\tan\left[\arcsin\left(n(\lambda)\sin\left(A - \arcsin\left[\frac{\sin(\alpha_c + \arctan(\frac{x_0}{F}))}{n(\lambda)}\right]\right)\right) - \alpha_c\right] \tag{5}$$

This equation gives a point to point mapping between a 'pixel' at the scene and a mirror location at the DMD, where we have neglected the point spread function (PSF) of the system. Similarly, the mapping between the DMD and the camera is given by

$$x_2(\lambda, x_1) = F\tan\left[\arcsin\left(n(\lambda)\sin\left(A - \arcsin\left[\frac{\sin(\alpha_c + \arctan\left(\frac{x_1}{F}\right))}{n(\lambda)}\right]\right)\right) - \alpha_c\right] \tag{6}$$

By inserting Equation (5) into (6) we find

$$x_2(\lambda, x_0) = x_0 \tag{7}$$

Which mathematically demonstrates the property of colocation; a location on the scene corresponds exactly to a location on the camera, independent of wavelength. This result also implies that distortion arising due to the prism only influences the dispersed relay image in the DMD plane, and does not distort the final image in the camera plane.

3.2. Calibration Procedure

Due to the folding of the system the scene and camera planes are equivalent (see Equation (7)), and therefore we do not need to calibrate the system between the scene and the DMD, only between the DMD and the camera. One way to perform the calibration is to use a scene which is uniformly illuminated with a known monochromatic wavelength λ. The programmable nature of the DMD allows us to systematically turn 'on' a mirror at location x_1, and measure which camera pixel x_2 receives the reflected light. Starting from the description of the ideal system given by Equation (6), the incident camera pixel x_2 is given by the following function

$$x_2(\lambda, x_1) = f_3\tan\left[\arcsin\left(n(\lambda)\sin\left(A - \arcsin\left[\frac{\sin(\alpha_c + \arctan\left(\frac{x_1}{f_2}\right))}{n(\lambda)}\right]\right)\right) - \alpha_c\right] \tag{8}$$

The values f_2, f_3 and α_c are parameters which must be determined via calibration. f_2 and f_3 correspond to the focal lengths of lenses L_2 and L_3 respectively, and should both be equal to $F = 200\,\text{mm}$. However, due to misalignment or differences between lenses, it is more accurate to calibrate using two separate parameters, f_2 and f_3. Similarly, the exact angle of incidence α_c needs to be found via calibration, which in turn informs us of the true central wavelength λ_c of the system. For our system, $A = 30°$ and $n(\lambda)$ is given by the Sellmeier equation for BK7.

It is more practical to define the horizontal location x_1 of a DMD mirror using mirror index i, illustrated in Figure 5, giving

$$x_1 = \frac{\Delta_{DMD}(i - i_0)}{\sqrt{2}} \tag{9}$$

Where the width of the mirror $\Delta_{DMD} = 10.8\,\mu\text{m}$. The index i_0 is the centre of the DMD, and should be on the optical axis. In fact, due to the small angle approximation a small misalignment between the centre of the DMD and the optical axis is tolerated by the calibration function (8), by a change in the effective central wavelength of the system λ_c. This allows us to fix $i_0 = (1920 + 1080)/2 = 1500$, for our DMD configuration.

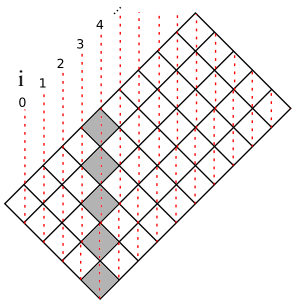

Figure 5: DMD configuration showing numbering convention i. Mirror rotation axis is vertical. The shaded squares show the mirrors turned to the 'on' position for $i = 4$, approximating a slit.

In our case, instead of using one, or several monochromatic sources, we use a fluorescent lamp with three sharp, well-separated and easily identifiable spectral peaks, shown in Figure 6a, which are used as reference wavelengths. This lamp is used to illuminate the entire scene. The calibration procedure is as follows; a column of mirrors or 'slit' is opened at location i on the DMD, and the image on the camera is recorded. The measurement is repeated until we have a camera image for every slit position i. Figure 6b shows an example of the image on the camera when the DMD slit is at $x_1 = 0$ ($i = i_0$). In the horizontal direction we see the spectrum of the lamp, with longer wavelengths to the left hand side. The three spectral peaks are clearly resolvable, allowing us to calibrate three separate wavelengths simultaneously. In Figure 6b, there is a slight curvature to

the lines in the vertical direction, a distortion effect which is discussed further in Section 3.3. To perform the initial calibration using Equation 8, we use the centre row of pixels on the camera at ($y_2 = 0$). For each DMD slit location x_1, the position x_2 of the three sharp spectral peaks are found with sub-pixel accuracy via parabolic approximation [23]. This gives a two-dimensional data set which is fit to Equation (8) using a least squares estimation.

The fit parameters are given in Table 1, with errors found by the 95% confidence interval of the fit. The values for f_2 and f_3 are within 3% of the expected value of 200 mm. The value found for α_c gives an effective central wavelength of $\lambda_c = 550.6$ nm. The calibrated spectrum for three different camera locations is shown in Figure 6c. Figure 6d gives the difference between the fitted curve and the measured data for the three wavelength peaks, showing a sub-pixel accuracy of the fit over the camera width, and an average error of 1.3 μm. As there is no obvious trend in the error with x_0, we conclude that noise is the main contributing factor, and we have no significant distortion or aberration in the lenses.

Parameter	Value	Error	Units
α_c	23.14	4.71×10^{-4}	$\circ$
f_2	201.5	0.141	mm
f_3	204.3	0.137	mm

Table 1: Fitted calibration parameters for Equation (8). Error is given by the 95% confidence interval of the fit.

The wavelength bands are defined by the DMD mirrors, and due to the non-linear dispersion of the prism the spectral bandwidth depends on the wavelength, ranging from 0.5 - 2.5 nm as demonstrated in Figure 7. Additionally, due to the dependence of the angle of incidence on the scene location x_0, the physical width of the spectrum on the DMD varies depending on the pixel location on the camera. In other words, the spatial spreading on the DMD, i.e. the distance $|x_1(\lambda = 400\,nm) - x_1(\lambda = 700\,nm)|$ depends on the position x_2, which in principle could influence the definition of the spectral bands. Our system has a small field of view, so likewise there is small variation in the angle of incidence α, resulting in a variation of only about 1.5% in the spectral width over the scene (see Figure 8). This small error can be ignored, and all the camera locations are assumed to have the same spectral bands. For systems with a larger field of view some post processing may be required to ensure that all the pixels in the hyperspectral datacube are defined using the same wavelength bands. According to Figure 8, the whole spectrum is spread on average over approximately 2.055 mm. For light originating from a single point on the scene, the spectral spreading at the DMD means there are $\sqrt{2} \times 2.055/\Delta_{DMD} \simeq 269$ columns of DMD mirrors between light at 400 nm and 700 nm.

3.3. Smile Distortion

As is apparent from Figure 6b, a vertical slit on the DMD is distorted to a curve in the plane of the camera. This well-known effect originates from the

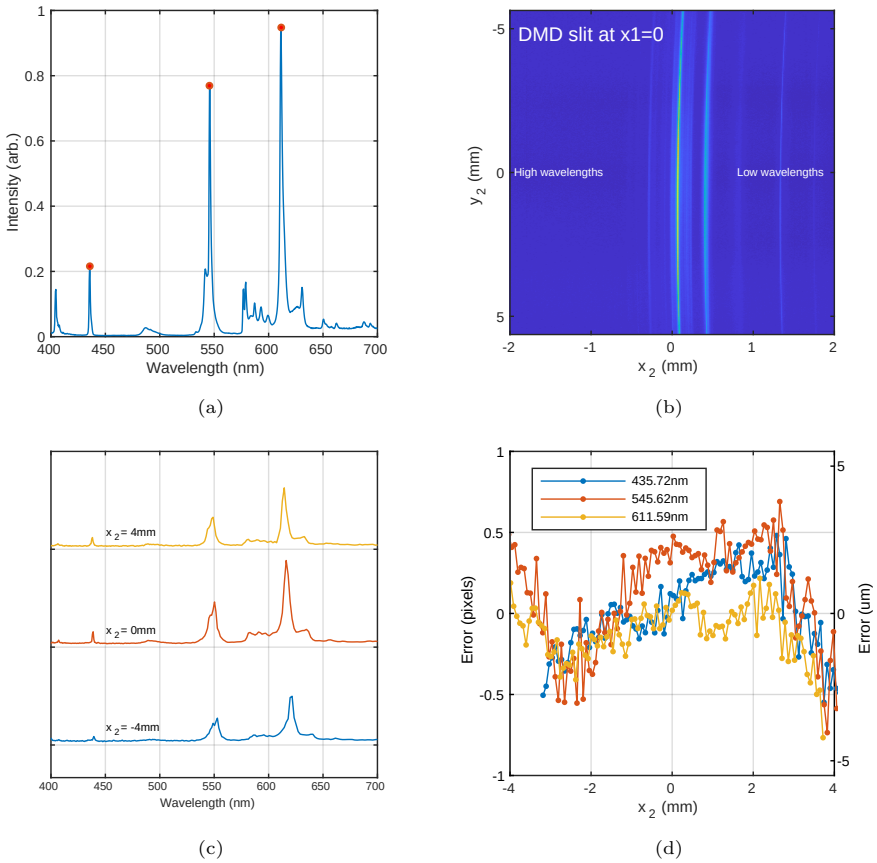

Figure 6: a) Spectrum of fluorescent lamp, red points mark the three peaks used as reference wavelengths to calibrate the system, b) Image on the camera when a DMD mirrors at $x_1 = 0$ are 'on', c) Calibrated spectrum for 3 camera locations, offset in y axis for clarity, d) The difference between the fit to Equation (8) and the measured data, for the three reference peaks.

prism [24], and is often termed 'smile distortion' in the hyperspectral imaging community [25]. This distortion only influences the image at the DMD plane; the second pass through the prism undoes this distortion, and there is no resulting spatial or spectral distortion between the scene and camera (see Appendix A). However, smile distortion does influence the spatio-spectral filtering applied to the scene by the DMD, and needs to be included in the calibration model.

The distortion is easily explained via ray-tracing, presented in the Appendix B, and arises due to the vertical angle of incidence to the prism. For our system, the small field of view allows the effect of this distortion to be simply represented as a shift in the camera pixel x_2 for a given DMD slit location x_1,

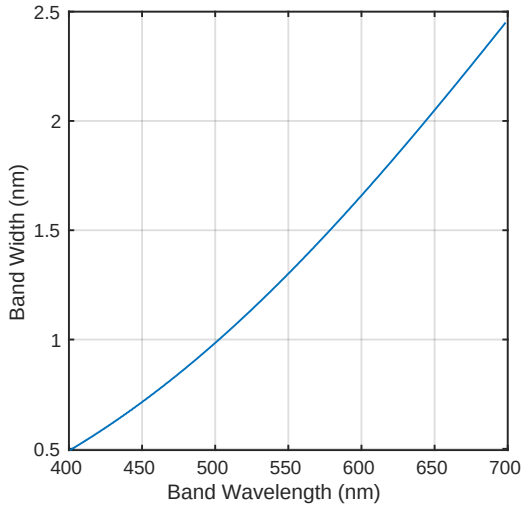

Figure 7: Width of spectral band, dependent on band wavelength, where one DMD mirror encodes one band.

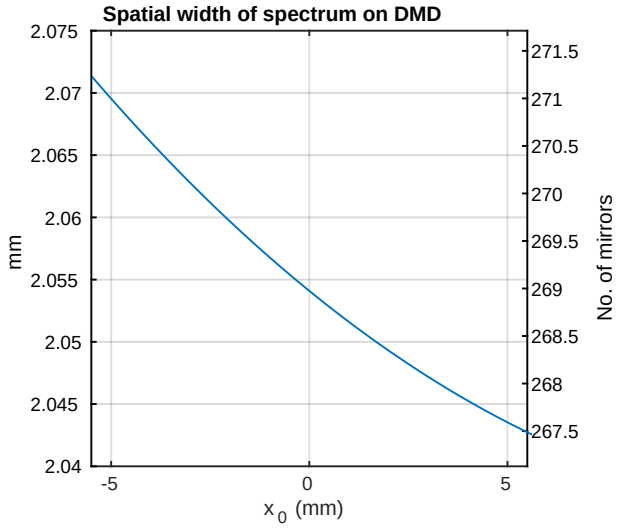

Figure 8: Spatial spreading on the DMD of the whole spectral band 400-700 nm, depending on the scene/camera pixel location. The width is determined by taking the inverse of Equation 8, as is equal to $|x_1(400\,nm, x_2) - x_1(700\,nm, x_2)|$.

depending on the vertical coordinate on the camera y_2;

$$x_2(\lambda, x_1, y_2) = x_2(\lambda, x_1) + f(y_2) \tag{10}$$

Where $f(y_2)$ can be approximated as a quadratic function, and is independent of wavelength and x_2:

$$f(y_2) = S(y_2 - y_s)^2 - Sy_s^2 \tag{11}$$

The parameter y_s gives the location of the centre of the smile in y, giving $f(0) = 0$. The value for S can be calculated using the theory presented in Appendix B, which gives $S = 1.2042\,/\mathrm{m}$, or can be determined by fitting to the measured data, as in Figure 9, which gives $S = 1.2048\,/\mathrm{m}$, as expected.

In our case this function gives a variation of less than $40\,\mu$m or roughly 7 pixels over the entire camera. For systems with larger field of view the influence of distortion becomes increasingly wavelength dependent, and a more complex model may be needed.

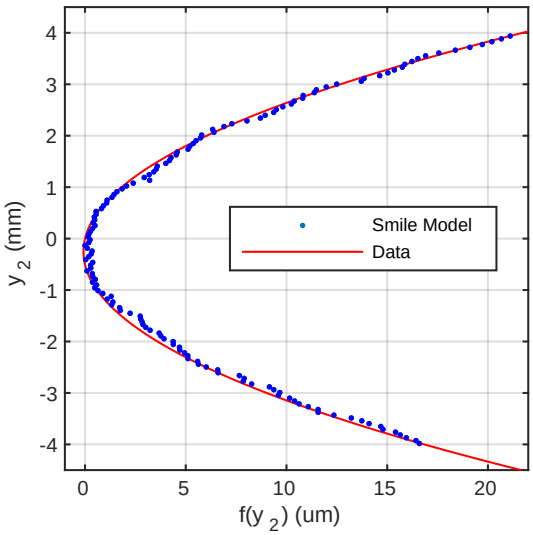

Figure 9: Smile distortion, blue dots show measured data, and red curve is the fit to quadratic function given by Equation (11), where $S = 1.2048\,/\mathrm{m}$ and $y_s = -227\,\mu$m.

4. Datacube Acquisition and Reconstruction

4.1. Scene definition and acquisition scheme

Bench-marking of the system is performed using a slit-scanning acquisition scheme, tested on a simple hyperspectral scene. A chrome on glass chequerboard target is illuminated from behind with a white LED, and from the front with the fluorescent lamp. The LED has a broad smooth spectrum, whilst the lamp has several sharp fluorescence peaks; the same lamp was used to calibrate the

device, and has spectrum shown in Figure 6a. Additionally, a HeNe laser beam ($\lambda = 633\,\text{nm}$) passes through a pinhole to illuminate a small region of the image, and the camera pixels are saturated in that region. A bandpass filter in the range 450-650 nm is placed before the first lens to remove background light, and provide some padding at either end of the spectrum.

The hyperspectral scene has distinct spatial regions with different spectra and intensity. The panchromatic image is shown in Figure 10b, with the different spectral regions labelled. The region of interest for the subsequent analysis is shown by the black box.

The slit-scanning acquisition scheme implemented here follows this approach; a column of mirrors is opened on the DMD, and the image on the camera is recorded. For the next acquisition, the slit is shifted by its width, and so on for the next measurement. Due to the configuration of the DMD, the 'slit' is approximated by a column of 'diamonds' or by the combination of several columns of diamonds, illustrated in Figure 10a. For each acquisition multiple slits are opened on the DMD, separated by the spatial extent of the spectrum (269 mirrors), so that multiple optical components are measured in parallel without overlap. This means that the number of acquisitions required to retrieve the whole cube is the same as the number of bands.

An example of the image registered on the camera for a single acquisition is shown in Figure 10c. Increasing the width of the slit by combining several columns degrades spectral resolution, but allows faster exposure time by increasing the light throughput per acquisition, and requires a decreased number of acquisitions. The re-configurability of the DMD allows the user to select the best slit-width for the scenario, depending on light levels, required resolution and SNR.

4.2. Direct cube reconstruction

For the following explanation it is preferable to move from continuous variables (x_n, y_n) to the discrete indexes defining the camera pixel or DMD mirror location. The DMD mirror index i is defined previously in equation (9), and the camera pixels are defined by the notation (r, c) for rows and columns, given by

$$r = \frac{x_2}{\Delta_{cam}} + 1024, c = \frac{y_2}{\Delta_{cam}} + 1024, \tag{12}$$

Where $\Delta_{cam} = 5.5\,\mu\text{m}$. To reconstruct the hyperspectral data cube from the camera acquisitions, consider a single scene pixel at (r, c), having ground truth discretized spectrum $\boldsymbol{o}$ of length N_λ, where N_λ, is the number of wavelength bands. For a particular acquisition n, the measured intensity of the pixel on the camera is given by m_n. The pixel value for several acquisitions is given by array $\boldsymbol{m}$ of length N_M, where N_M is the number of measurements. We have

$$\boldsymbol{m} = \boldsymbol{H}\boldsymbol{o} \tag{13}$$

The matrix $\boldsymbol{H}$ defines the spectral filtering implemented by the DMD, and depends on the DMD mask applied for each acquisition. We also assume uniform

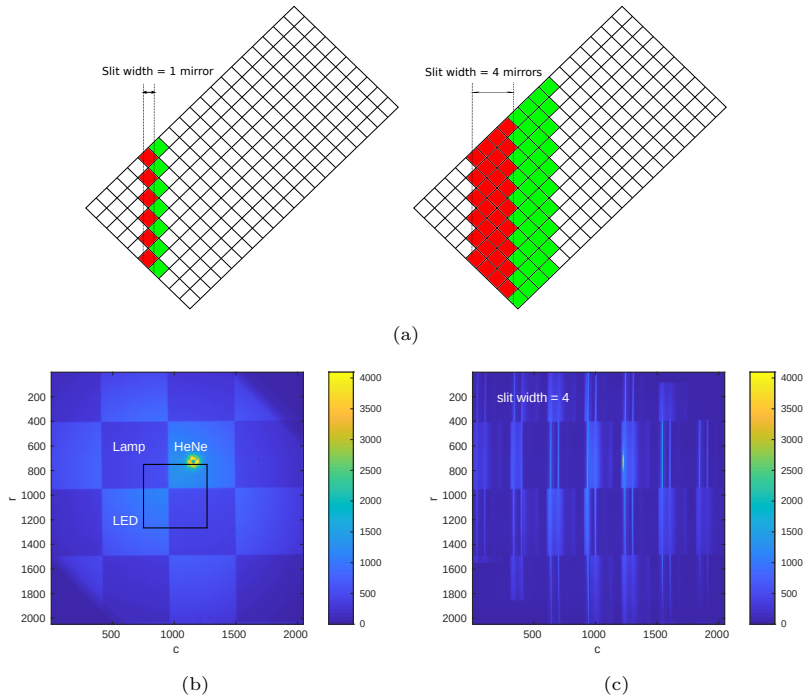

Figure 10: a) Schematic of a slit on the DMD, left Figure has slit width = 1, right, width = 4. Red shows position of the slit for the first acquisition, green for the second acquisition, b) Panchromatic image of hyperspectral scene, taken with all mirrors open, c) Image recorded on camera for single acquisition of slit scanning scheme with slit width = 4, exposure time 25 ms.

quantum efficiency over the spectral range, and ignore any contribution due to noise or dark values on the pixel.

The wavelength bands for the discretized spectrum $\boldsymbol{o}$ are defined in the frame of the DMD, and depend on the slit width. For the slit-scanning acquisition scheme we have $N_\lambda = N_M$, and it should be clear that matrix H has the form of an identity matrix, since for each acquisition only one spectral band per pixel is reflected back to the camera.

$$\boldsymbol{H} = \begin{bmatrix} 1 & 0 & 0 & \dots \\ 0 & 1 & 0 & \dots \\ 0 & 0 & 1 & \dots \\ \vdots & \vdots & \vdots & \ddots \end{bmatrix} = \boldsymbol{I} \tag{14}$$

It is therefore straightforward to determine the spectra of the pixel, via

$$\boldsymbol{o} = \boldsymbol{I}^{-1}\boldsymbol{M} = \boldsymbol{m} \tag{15}$$

to ensure that the wavelength bands are the same for all pixels, ensuring that the datacube is regular, a constraint which makes the datacube easier to interpret

and analyse. For example, it is often desirable that a user can easily access a monochromatic image. The wavelength bands for the whole cube are defined using a reference pixel, in our case at the centre of the image $(r, c) = (1024, 1024)$. The bands λ_n are determined by using the calibration functions to find the wavelengths incident on the DMD mirrors i, which are illuminated over the spectral range of interest. For every other pixel location on the camera, the calibration functions are used to determine which DMD slit location encodes each of these wavelength bands. The array $\boldsymbol{m}$ in equation (15) can be circularly shifted depending on the camera pixel, to compensate for the slit location change for each measurement. As we have demonstrated in Section 3 (Figure 8), the number of DMD mirrors required to encode the full spectrum is approximately the same over the entire camera. This is another feature that ensures the datacube measured is regular and easy to interpret. As there is not a one-to-one relationship between the slit width and the camera pixel width, the calibration functions will typically return a non-integer index for the relevant DMD mirror, indicating that the wavelength bands defined by the reference pixel do not ideally overlap with the DMD mirrors for the majority of the pixels. In this case, the result is rounded to find the nearest DMD mirror which matches the reference wavelength band, allowing us to approximate $\boldsymbol{H} = \boldsymbol{I}$. As we will see later, this approximation causes non-trivial problems in monochromatic image quality.

4.3. Issues with the direct reconstruction scheme

The scene was measured using the slit-scanning technique with slit width 1 mirror wide, encoding 269 bands, with exposure time of 100 ms, and subsequently with slit width of 4 mirrors, encoding 67 bands with exposure time of 25 ms. The hyperspectral datacube was reconstructed using equation 15.

A monochromatic image of the region of interest is shown in Figures 11a and 11c, for the wavelength band which contains the sharp spectral peak of the fluorescent lamp. The centre wavelength of each spectral band changes depending whether the slit width is odd or even, so for slit width of 1 the band centre for the monochromatic image is 609 nm, whilst for slit width of 4 it is 608 nm. Figures 11b and 11d show a cross-section through the datacube, giving the spectrum dependent on camera pixel c, when $r = 900$. The region illuminated from behind via the LED also contains a contribution from the fluorescent lamp - due to reflection from the glass. Observing the monochromatic images, it is immediately apparent that there is a periodic 'artifact' which is most obvious in the region illuminated by the fluorescent lamp. The origin of this artifact arises from a periodic error in the spectrum, shown in Figures 11b and 11d, which has spatial frequency dependent on the slit width. In the monochromatic image, the artifact is much more visually obvious for regions that have sharp spectral features.

The root cause of the artifact originates from the assumption that $\boldsymbol{H} \approx \boldsymbol{I}$ for all pixels, which we approximate by rounding up or down to find the index of the nearest DMD mirror which matches the reference wavelength bands. Figure 12 illustrates the cause of this problem more clearly; the reference pixel

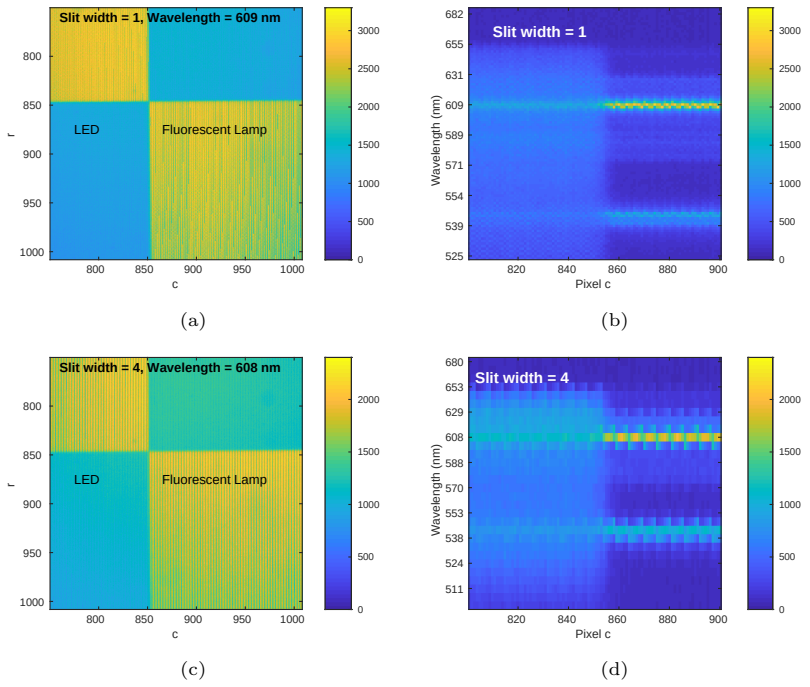

Figure 11: a) Monochromatic image reconstructed using slit width of 1 and b) sub-section of spectrum for r=900, c) monochromatic image reconstructed using slit width of 4 and d) sub-section of spectrum for r=900.

B has bands which are perfectly encoded by the DMD slit pattern, but adjacent pixels A and C are offset by less that the slit width. When a particular slit is open, the measurement value m_n for pixels A and C are thus a mixture of the spectral bands defined by B. The exact combination depends on the distance of the offset d. This problem gets worse as the slit width W increases relative to the pixel size, as we can observe by comparing Figure 11a and Figure 11c, noting the spatial frequency of the banding.

Although this offset causes an error in spectral measurement, and periodic artifacts in monochromatic images, it is not often mentioned in the literature. One point of note is that hyperspectral imagers are often tested using broader spectral sources which reduce the visibility of these artifacts [26, 17]. It is only by trying to measure sharp spectral features that the problem becomes apparent. There has been some discussion on correcting this offset for the particular case of Hadamard hyperspectral imagers [9, 12, 10], however it is useful to study the problem for even simpler acquisition schemes to understand a variety of approaches which could be applicable to a wider range of acquisition schemes.

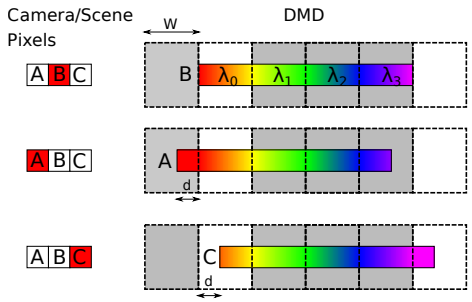

Figure 12: The spectral banding in the reconstructed hyperspectral data cube, for $N_\lambda = 4$. Note that the irregular shape of the slit is neglected in this diagram for simplicity.

5. Artifact Correction

There are a few simple methods to correct the periodic artifact arising from the mismatch between the camera pixel and the DMD slit. Depending on the scenario one approach may perform better that another, as the artifact is influenced by many factors; slit width, the relative size between mirror and pixel, point spread function, resolution, and the 'sharpness' of the spectral features in the scene, are all factors which come into play. Another concern to consider is the extra computational time needed to reconstruct the corrected cube for each method.

In the following sections we examine the performance of the various approaches for the case where the slit width is 4 mirrors wide; the artifact in this case is more significant and it will be easier to assess the results of the different methods. These techniques are applied here only to a slit scanning type acquisition scheme - but it should be clear where they may be extended to other types of acquisition schemes.

5.1. Pixel Binning and Averaging

To begin with, an obvious approach would be to group the camera pixels together into 'super-pixels', which are the same size as the slit width implemented on the DMD. For example, in the case of Figure 12 we would sum the pixel intensity measured at pixel B and its neighbours to the left and right. The obvious drawback with this method is the loss in spatial resolution, albeit in one direction only, as we only need to consider the direction of dispersion - along the horizontal axis. Pixel binning has been used in some recent works, [19, 17], although with little discussion of the advantages or disadvantages.

Consider our case; we have a slit comprising of 4 mirrors, and with the DMD at a 45° angle, this gives a slit width of $4 \times 10.8/\sqrt{2} = 30.55\,\mu$m, approximately 5.55 camera pixels wide. A non-integer binning method is used to combine 5.55 pixels in the horizontal direction, with the results shown in Figure 13. In the binned image, the artifact has almost completely vanished, but at a detriment to the spatial resolution. Any remaining periodic structure in the image may arise

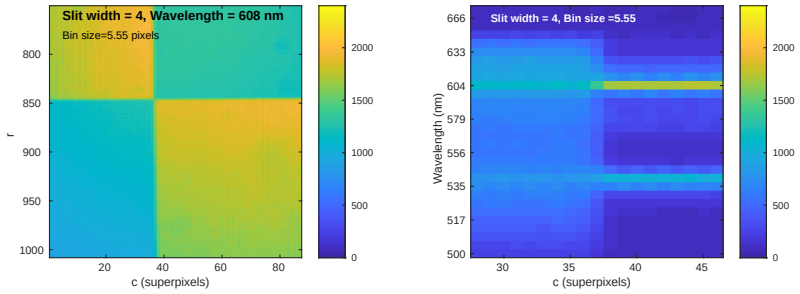

(a) (b)

Figure 13: a) Monochromatic image binned along c using non-integer bin size, b) spectrum vs super-pixel, where r=900.

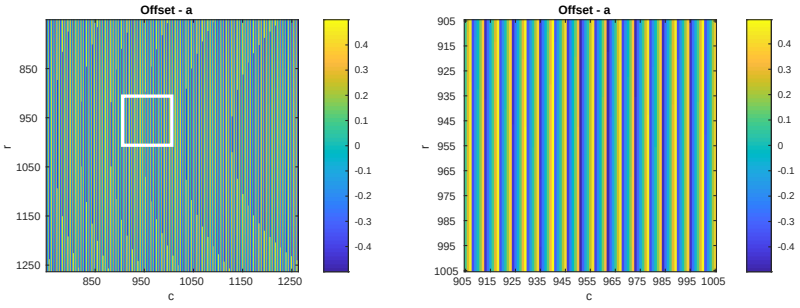

(a) (b)

Figure 14: a) Offset a for each camera pixel, determined by the calibration functions, b) close up on region marked by white box.

due to the combination of two periodic features (i.e. the image and the binning), resulting in another periodic artifact - similar to a Moire effect. Whilst this simplistic approach has drawbacks, it is easy to implement and does not require accurate knowledge of the system itself - any datacube with periodic artifacts could be binned to reduce them. One could experiment with increasing the bin size until the artifacts are eliminated, but at the cost of a degraded spatial resolution.

5.2. Linear Interpolation

The previous method using binning inevitably results in a loss of information in the datacube. To maintain accuracy, lets consider that the pixels which are offset are being simply measured using a different wavelength basis to the reference pixels. According to Figure 12, we define $a = d/W$ as the fractional offset, where the sign of a gives the direction of the offset, so $-0.5 \geq a > 0.5$. By using linear interpolation we can thus find the measured spectrum in the wavelength basis of the reference pixel, via

$$\boldsymbol{o}_{interpolated} = (1 - |a|)\boldsymbol{o} + |a|\boldsymbol{o'} \tag{16}$$

Where $\boldsymbol{o'}$ is the reconstructed matrix $\boldsymbol{o}$, cyclically shifted by plus or minus one, depending on the sign of a. The interpolation method assumes approximately linear dispersion over each band, which is reasonable so long as the band width is small enough. The first and last bands will not be reconstructed correctly, so should not contain any useful spectral information.

The value for a must be as accurate as possible, and is found by using the calibration functions. For slit width of 4 mirrors, a is shown in Figure 14 over the region of interest. Comparing this Figure to Figure 11c, the close correspondence between the patterns makes it clear that the offset is the origin of the artifact.

The monochromatic image for the corrected datacube is shown in Figure 15a, with the spectral cross-section shown in Figure 15b. The contrast of the artifact has been reduced, but some periodicity remains; this is expected due to typical problems interpolating data with sharp peaks. Applying this method requires highly accurate calibration, although the advantage is we maintain much of the original information in the data cube, and remain true to the ground truth spectrum without loss of resolution. More advanced methods of interpolation could be implemented, at a detriment to the computation time.

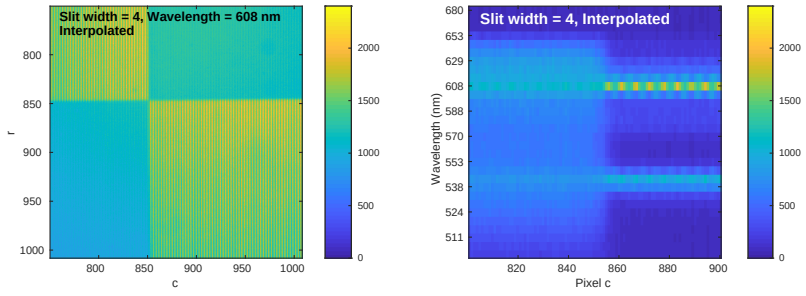

(a) (b)

Figure 15: Data from reconstructed hyperspectral data cube, corrected via interpolation method. a) Monochromatic image from acquisition data taken with slit width of 4, b) section of spectrum for r=900, for slit width 4.

5.3. Matrix Correction

The final method to correct this artifact delves further into the properties of the filtering matrix $\boldsymbol{H}$ which is applied by the DMD spectral filter. Using the same definition for offset a as the previous section, the actual filtering matrix $\boldsymbol{H}$ for $a \leq 0$ is given below

$$\boldsymbol{H}_{a<0} = \begin{bmatrix} 1-|a| & |a| & 0 & \dots & 0 \\ 0 & 1-|a| & |a| & \dots & 0 \\ 0 & 0 & 1-|a| & \dots & 0 \\ \vdots & \vdots & \vdots & \ddots & \vdots \\ |a| & 0 & 0 & \dots & 1-|a| \end{bmatrix} \tag{17}$$

For values of $a > 0$, $\boldsymbol{H}$ is the matrix $\boldsymbol{H}_{a<0}$ mirrored along the diagonal. In the original reconstruction method we approximate $\boldsymbol{H}^{-1} \approx \boldsymbol{I}$ by rounding a to zero. The actual matrix $\boldsymbol{H}^{-1}$ is poorly conditioned as $|a|$ approaches 0.5. As $|a|$ increases, the matrix $\boldsymbol{H}^{-1}$ transitions from a sparse diagonal matrix to a matrix with many significant terms. As such, when a is non zero, determining the spectrum via $\boldsymbol{o} = \boldsymbol{H}^{-1}\boldsymbol{m}$ requires the combination of many measurement values m_n to find each spectral band o_n, which amplifies the noise and produces inaccurate results. Furthermore, when $|a| = 0.5$ the matrix $\boldsymbol{H}$ is non-invertible.

If we consider the measurements from a pixel which has offset $a = -0.5$, we find that each measurement value is the average of two spectral bands defined by the reference pixel:

$$m_n = \frac{1}{2}(o_n + o_{n+1}) \tag{18}$$

In other words, the spectral bands for the pixel lie halfway between each slit open on the DMD. In this case, it is impossible to manipulate the acquisition data to obtain more information about the spectrum (hence why for this case $\boldsymbol{H}$ is singular).

Instead of trying to find the ground truth spectrum $\boldsymbol{o}$ from the measurement values $\boldsymbol{m}$, we could instead try to find the approximate spectrum $\tilde{\boldsymbol{o}}$, where each spectral band $\tilde{o}_n$ is actually the average of the two original spectral bands.

$$\tilde{o}_n = \frac{1}{2}(o_n + o_{n+1}) \tag{19}$$

This matches the measurement made when the pixel is halfway between mirrors. So we now have

$$\tilde{\boldsymbol{o}} = \frac{1}{2}\begin{bmatrix} 1 & 1 & 0 & \dots & 0 \\ 0 & 1 & 1 & \dots & 0 \\ 0 & 0 & 1 & \dots & 0 \\ \vdots & \vdots & \vdots & \ddots & \vdots \\ 1 & 0 & 0 & \dots & 1 \end{bmatrix} \boldsymbol{o} = \boldsymbol{X}\boldsymbol{o} \tag{20}$$

Where is should be clear that $\boldsymbol{X} = \boldsymbol{H}(\boldsymbol{a = -0.5})$. The array of measurements can now be expressed by

$$\boldsymbol{m} = \boldsymbol{H}\boldsymbol{o} = \boldsymbol{H}\boldsymbol{X}^{-1}\tilde{\boldsymbol{o}} = \boldsymbol{G}\tilde{\boldsymbol{o}} \tag{21}$$

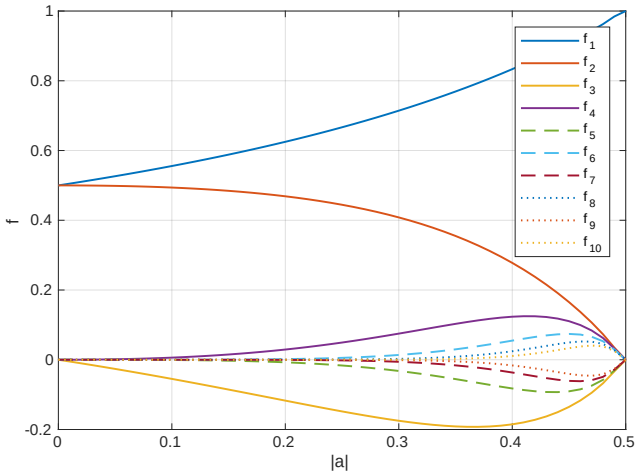

Figure 16: First ten values of f_n, in $\boldsymbol{G^{-1}}$, as a function of $|a|$.

To find the approximate spectrum $\tilde{\boldsymbol{o}}$ from the measurements requires an inversion of the matrix $\boldsymbol{G} = \boldsymbol{H}\boldsymbol{X^{-1}}$.

$$\tilde{\boldsymbol{o}} = \boldsymbol{G^{-1}}\boldsymbol{m} \tag{22}$$

In turns out that the matrix $\boldsymbol{G}$ is a much easier matrix to work with than $\boldsymbol{H}$, as it is always invertible and the inverted matrix never contains a large number of significant terms. Representing the terms of the matrix by a function f_n which is dependent on a, $\boldsymbol{G^{-1}}$ is given by

$$\boldsymbol{G^{-1}_{a>0}} \approx \begin{bmatrix} f_1(a) & f_2(a) & f_3(a) & \dots \\ f_N(a) & f_1(a) & f_2(a) & \dots \\ f_{N-1}(a) & f_N(a) & f_1(a) & \dots \\ \vdots & \vdots & \vdots & \ddots \end{bmatrix}$$

$$\boldsymbol{G^{-1}_{a<0}} \approx \begin{bmatrix} f_2(a) & f_1(a) & f_N & \dots & f_3(a) \\ f_3(a) & f_2(a) & f_1(a) & \dots & f_4(a) \\ f_4(a) & f_3(a) & f_2(a) & \dots & f_5(a) \\ \vdots & \vdots & \vdots & \ddots & \end{bmatrix} \tag{23}$$

For all values of a we have $|f_n(a)| > |f_{n+1}(a)|$, and many of the terms are extremely small; which greatly reduces the influence of noise. The first ten terms of the matrix are shown in Figure 16, for the case where there are 55 spectral bands. As a sanity check, we see that when $a = -0.5$ the matrix $\boldsymbol{G^{-1}} = \boldsymbol{I}$ and when $a = 0$ we have $\boldsymbol{G^{-1}} = \boldsymbol{X}$.

This method effectively degrades the spectral resolution by a factor 2, although the number of bands remains the same. The wavelength bands for $\tilde{\boldsymbol{o}}$ are also shifted by half a bandwidth compared to $\boldsymbol{o}$.

The matrix $\boldsymbol{G}$ is used to reconstruct the spectral datacube from the acquisition data, with the results shown in Figure 17. We observe a better reduction in the contrast of the periodic artifact compared to interpolation, but the fluorescence peak has been broadened. This method remains as close to the ground truth as possible - there are no approximations made in the analysis of the data, and similarly to interpolation, this method requires accurate calibration settings to perform well.

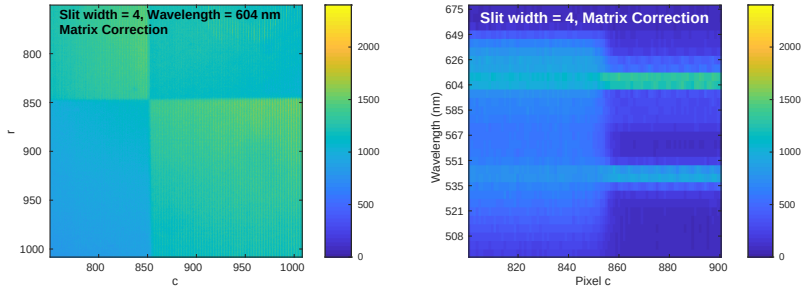

(a) (b)

Figure 17: Data from hyperspectral data cube constructed using $\boldsymbol{G}$ a) Monochromatic image from acquisition data taken with slit width of 4, b) section of spectrum for r=900, for slit width 4.

5.4. Artifacts Arising from Diamond-shaped Micro-mirrors

Another more minor artifact occurs due to the orientation of the DMD. Due to the 45° rotation, a 'slit' on the DMD is actually a column of diamonds, and thus has a variable width (see Figure 10a). The slit scanning acquisition scheme approximates the column as a rectangular slit. This approximation is not accurate for narrow slit widths, and leads to a two-dimensional periodic pattern in the reconstructed data cube. Figure 18a demonstrates this particular type of artifact in the monochromatic image of the uncorrected hyperspectral data cube, where the data was obtained with a slit width of 1 mirror wide. In this case the artifact is clear even for regions which are illuminated with light with broad spectral features - here it shows up clearly for the region of the image illuminated by the LED. The contrast of this artifact is not high, although this depends on the PSF of the system and the relative sizes between the mirror and the pixel. In our system, for regions with sharp spectral features this artifact is dwarfed by the artifact caused by the offset a. In the monochromatic image, the spatial frequency of the artifact corresponds to the spatial frequency of the mirrors on the DMD, and as we see in the spectral plane Figure 18b the periodicity of the artifact is the same as the wavelength bands. Figure 18c uses the same acquisition data but reconstructs the monochromatic image using

matrix $\boldsymbol{G}$, which conveniently smooths the results and removes the artifact. This artifact could also be resolved by changing the orientation of the DMD, or using a larger slit width.

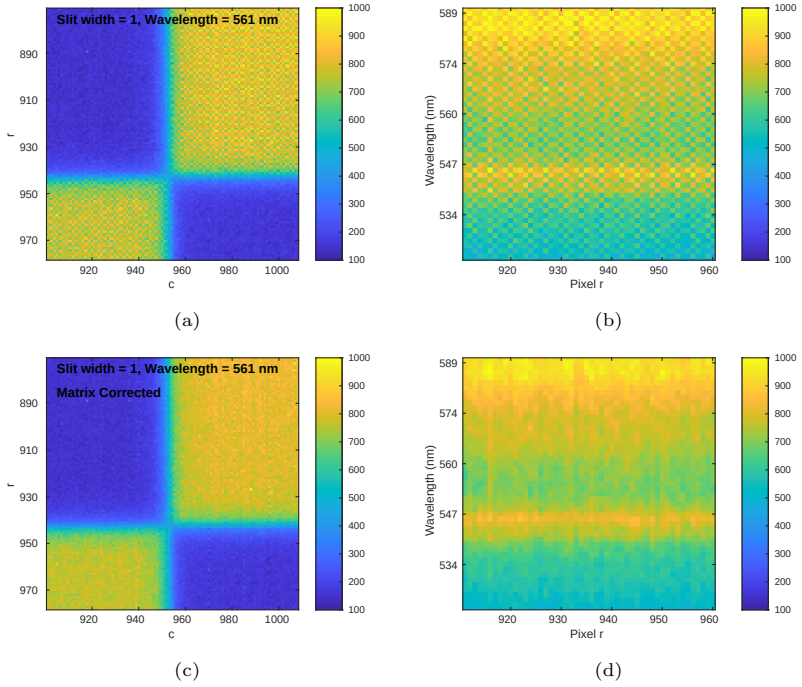

Figure 18: Section of reconstructed datacube of size 100 by 100 pixels, measured with slit width of 1, a) Uncorrected monochromatic image b) section of spectrum for c=980, c) monochromatic image reconstructed using $\boldsymbol{G}$, d) section of spectrum for $c = 980$

5.5. System design

These artifacts arise mainly from the difference in size and shape of the DMD mirror and the camera pixel. Ideally, one could select a camera and a DMD which have identical pixel dimensions, but the range of commercially available hardware is limited. An alternative method would be to tune the magnification ratio of lenses L_2 and L_3 so the imaged DMD mirror corresponds to the pixel size on the camera. Even in this case, optical distortion in the prism causes misalignment between the pixel and mirror over the surface of the camera, although this could be reduced by using a less distortive dispersive element such as a grating. Eliminating the artifacts by changing the components places constraints on the system design, and therefore it may be simpler to address these issues by accurate calibration and post-processing, implemented by dedicated signal processing hardware.

6. Results

6.1. Spectral Resolution and Transmission

Figure 19 compares how the measured spectrum differs with slit width, when the exposure time is the same. Wider slits allow more light to reach the camera, resulting in an improved SNR, although spectral resolution is degraded. As is apparent from Figure 19b, the shape of the spectrum seems to differ with the slit width, as is particularly obvious in the region from 525 to 625 nm. In Figure 20a, the three spectra have been rescaled according to the slit width, and shown in comparison to the ground truth spectrum.

The shape of the transmission efficiency spectrum is then found by taking the ratio between the ground truth spectrum and the measured spectrum, and is shown in Figure 20b. We see that the transmission spectrum depends on the slit width itself. The origin of this effect is due to the properties of the DMD; the DMD is essentially a periodic array of tilted mirrors, and therefore acts as a grating, meaning that the transmission efficiency can vary with wavelength [27]. The difference in the transmission spectrum between a slit width of 1 and 2 is particularly apparent, but as more mirrors are added to the slit the shape of the transmission spectrum stabilizes.

For a given system, the change in transmission due to the diffraction efficiency will depend on several factors; including the angle of the optical axis to the DMD, the NA of the lenses, and also the acquisition scheme itself (for example the number of mirrors opened per acquisition). For most cases it may be simpler to determine the shape of the transmission spectrum empirically on a case by case basis.

6.2. Monochromatic Images

Now that the artifacts have been corrected and the transmission efficiency has been determined, we can use the system as a hyperspectral imager. The test scene consists of a chrome on glass chequerboard, illuminated from the front with a fluorescent lamp, and from behind with an LED, with a HeNe laser illuminating a small region. The panchromatic is shown in Figure 10b. The acquisition data was obtained using a slit-scanning scheme, with a slit width of 2. The exposure time for each acquisition was 50 ms. A slit width of 2 gives a good compromise between spectral resolution and SNR, and also gives a good compromise between the two different types of artifacts detailed in section 5. The datacube was reconstructed using the matrix correction method outlined in section 5.3.

Selected monochromatic images for the entire camera are shown in Figure 21. Figure 21a at the HeNe laser wavelength shows the laser spot clearly, which is not present in the other monochromatic images. Figure 21b shows the scene at a wavelength corresponding to the brightest spectral peak of the fluorescent lamps, which is reflected from the metallic parts of the mask. At the wavelength band shown in Figure 21c the spectral intensity of the LED and the lamp are very close, so the chequerboard pattern is hardly visible. In Figure 21d, the spectral intensity of the LED is much stronger than the lamp, so we see the

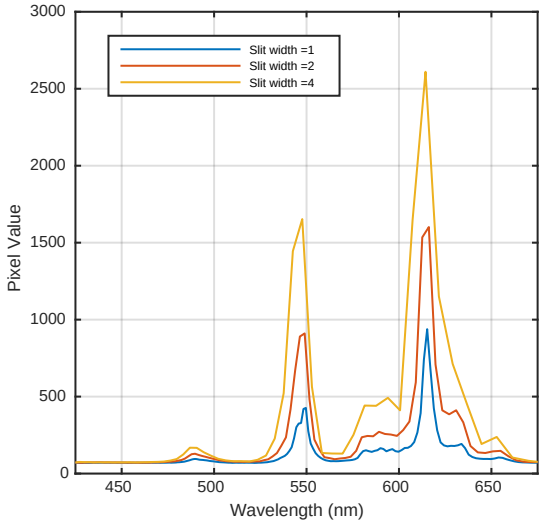

(a)

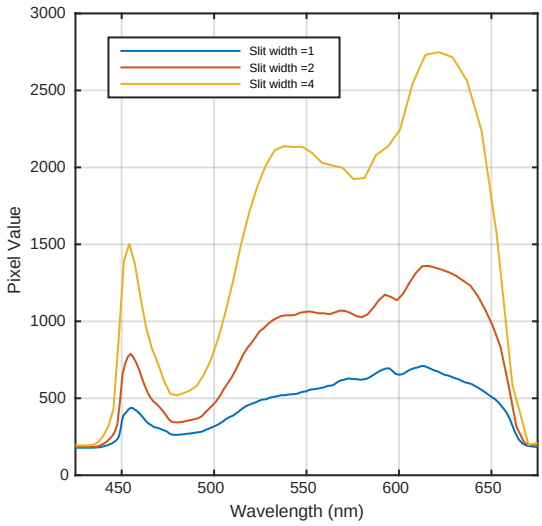

(b)

Figure 19: Comparison of the spectrum measured with a slit width of 1, 2 and 4, for a) fluorescent lamp, with exposure time 15 ms and b) LED with exposure time 30 ms.

inverse of the chequerboard pattern in Figure 21c, as in this case the light from the LED is blocked by the metallic parts of the mask. In short, our results are as expected and show good spatial resolution with little evidence of any artifacts.

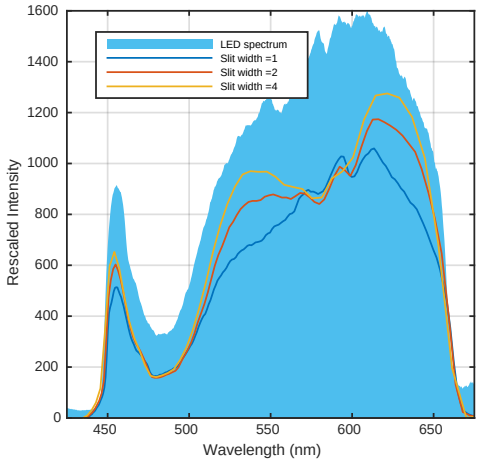

(a)

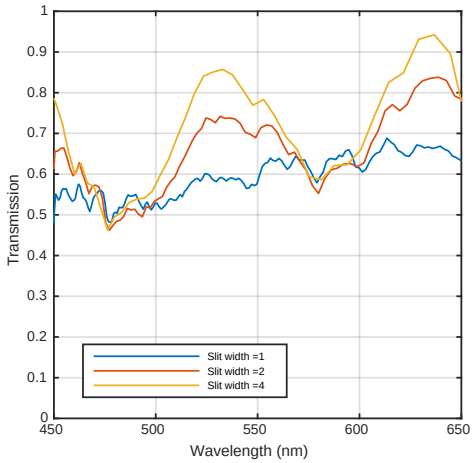

(b)

Figure 20: a) The measured LED spectra re-scaled with background level removed, and compared to the ground truth spectrum. b) the transmission efficiency as a function of wavelength, determined by taking the ratio between the measured spectrum and the ground truth (arbitrary units).

7. Conclusion

The hyperspectral imaging system presented here has been shown to generate accurate spectral data with a good spatial resolution. One of the advantages of this system is the small field of view, which limits distortion, and thus the modelling and calibration of the system is fairly straightforward. In terms of datacube reconstruction, we have addressed various issues arising from the use

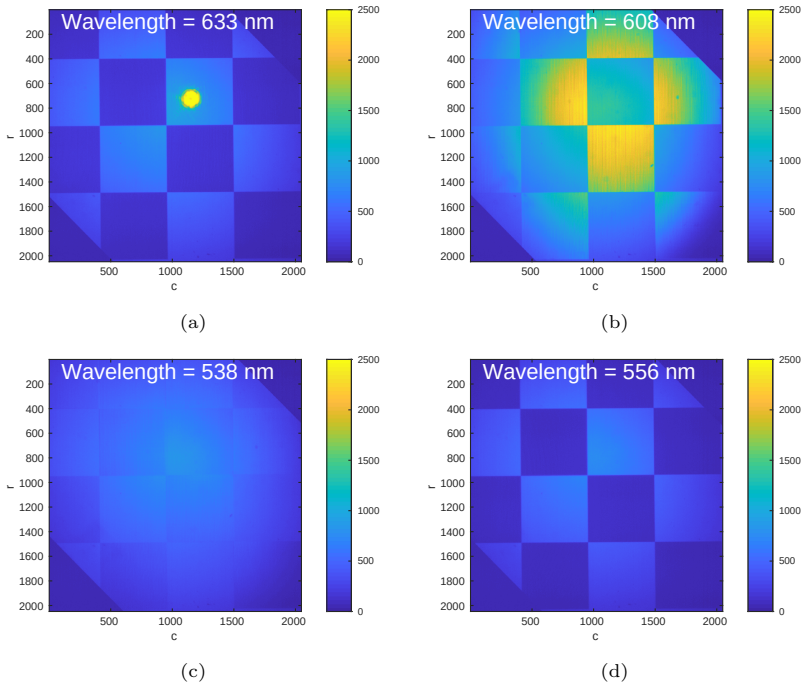

Figure 21: Monochromatic images from the reconstructed datacube, measured with slit width of 2 and exposure time 50 ms. Wavelength band a) 633 nm corresponding to HeNe laser wavelength, b) 608 nm corresponding to the strongest peak of fluorescent lamp, c) 538 nm where the spectral intensity of the lamp and LED are roughly equal, and d) 556 nm where the spectral intensity of the LED is much brighter than the lamp.

of the DMD, such as artifacts in the datacube, and a non-uniform transmission spectrum, and we give a few methods for resolving these issues.

The simple slit-scanning acquisition scheme described here provides a useful benchmark with which to compare more complex acquisition schemes. The property of colocation combined with the re-configurability of the DMD presents an interesting opportunity to develop an adaptive approach to datacube acquisition, and pursue near-snapshot spectral imaging. The system here is an ideal prototype to develop such methods.

References

[1] R. G. Sellar, G. D. Boreman, Classification of imaging spectrometers for remote sensing applications, Optical Engineering 44 (1) (2005) 013602.

[2] N. Hagen, Snapshot advantage: a review of the light collection improvement for parallel high-dimensional measurement systems, Optical Engineering 51 (11) (2012) 111702. doi:10.1117/1.OE.51.11.111702.

URL http://opticalengineering.spiedigitallibrary.org/article.aspx?doi=10.1117/1.OE.51.11.111702

[3] N. Hagen, M. W. Kudenov, Review of snapshot spectral imaging technologies, Optical Engineering 52 (9) (2013) 090901. doi:10.1117/1.OE.52.9.090901.
URL http://opticalengineering.spiedigitallibrary.org/article.aspx?doi=10.1117/1.OE.52.9.090901

[4] X. Dong, X. Xiao, Y. Pan, G. Wang, Y. Yu, Dmd-based hyperspectral imaging system with tunable spatial and spectral resolution, Opt. Express 27 (12) (2019) 16995–17006. doi:10.1364/OE.27.016995.
URL http://www.opticsexpress.org/abstract.cfm?URI=oe-27-12-16995

[5] X. Lin, G. Wetzstein, Y. Liu, Q. Dai, Dual-coded compressive hyperspectral imaging, Optics letters 39 (7) (2014) 2044–2047.

[6] R. Arablouei, E. Goan, S. Gensemer, B. Kusy, Fast and robust pushbroom hyperspectral imaging via dmd-based scanning, in: Novel Optical Systems Design and Optimization XIX, Vol. 9948, International Society for Optics and Photonics, 2016, p. 99480A.

[7] H. Rueda, H. Arguello, G. R. Arce, Dmd-based implementation of patterned optical filter arrays for compressive spectral imaging, JOSA A 32 (1) (2015) 80–89.

[8] S. P. Love, Programmable matched filter and Hadamard transform hyperspectral imagers based on micromirror arrays, in: L. J. Hornbeck, M. R. Douglass (Eds.), Emerging Digital Micromirror Device Based Systems and Applications, Vol. 7210, SPIE, 2009, p. 721007. doi:10.1117/12.808060.

[9] J. Xu, B. Hu, D. Feng, The correction of recovered spectral images in a hadamard transform spectral imager based on a digital micro-mirror device, Applied Spectroscopy 66 (9) (2012) 1044–1052. doi:10.1366/11-06577.

[10] J. Xu, Z. Zhu, C. Liu, Z. Huang, The processing method of spectral data in Hadamard transforms spectral imager based on DMD, Optics Communications 325 (2014) 122–128. doi:10.1016/j.optcom.2014.03.076.

[11] X. Sun, B. L. Hu, L. B. Li, Z. H. Wang, An engineering prototype of Hadamard transform spectral imager based on Digital Micro-mirror Device, Optics and Laser Technology 44 (1) (2012) 210–217. doi:10.1016/j.optlastec.2011.06.020.

[12] C. Ma, H. Lin, G. Zhang, R. Du, An efficient calibration method for multispectral imaging, Optics Communications 420 (2018) 14–25. doi:10.1016/j.optcom.2018.03.025.

[13] S. P. Love, D. L. Graff, Full-frame programmable spectral filters based on micromirror arrays, Journal of Micro/Nanolithography, MEMS, and MOEMS 13 (1) (2014) 011108. doi:10.1117/1.JMM.13.1.011108.
URL http://nanolithography.spiedigitallibrary.org/article.aspx?doi=10.1117/1.JMM.13.1.011108

[14] D. L. Graff, S. P. Love, Adaptive hyperspectral imaging with a MEMS-based full-frame programmable spectral filter, in: M. A. Druy, R. A. Crocombe (Eds.), Next-Generation Spectroscopic Technologies VII, Vol. 9101, SPIE, 2014, p. 910111. doi:10.1117/12.2051436.

[15] D. L. Graff, S. P. Love, Real-time matched-filter imaging for chemical detection using a DMD-based programmable filter, Proc. SPIE 8618, Emerging Digital Micromirror Device Based Systems and Applications V 8618 (March 2013) (2013) 86180F(1) – 86180F(10). doi:10.1117/12.2002694.
URL http://proceedings.spiedigitallibrary.org/proceeding.aspx?doi=10.1117/12.2002694

[16] D. L. Graff, S. P. Love, Real-time video imaging of gas plumes using a DMD-enabled full-frame programmable spectral filter, in: Emerging Digital Micromirror Device Based Systems and Applications VIII, Vol. 9761, 2016, p. 97610C. doi:10.1117/12.2211187.

[17] C. Ma, H. Lin, G. Zhang, R. Du, Digital micro-mirror device based multispectral imaging using compressed Fourier spectrum, Optics Communications 426 (2018) 348–358. doi:10.1016/j.optcom.2018.05.067.

[18] M. Dunlop, P. Jansen, D. Golish, M. Gehm, AFSSI-C: the Adaptive Feature-Specific Spectral Imaging Classifier, 2013, p. CM4B.4. doi:10.1364/cosi.2012.cm4b.4.

[19] M. Dunlop-Gray, P. K. Poon, D. Golish, E. Vera, M. E. Gehm, Experimental demonstration of an adaptive architecture for direct spectral imaging classification, Optics Express 24 (16) (2016) 18307. doi:10.1364/oe.24.018307.

[20] I. Ardi, H. Carfantan, S. Lacroix, A. Monmayrant, Fast hyperspectral cube reconstruction for a double disperser imager, in: 2018 26th European Signal Processing Conference (EUSIPCO), IEEE, 2018, pp. 2225–2229.

[21] T. T. Hill, Introduction to photographic principles (larmore, lewis) (1967).

[22] S. McGregor, S. Lacroix, A. Monmayrant, Adaptive hyperspectral imager: Design, modeling, and control, Journal of Optics (United Kingdom) 17 (8) (2015) 85607. doi:10.1088/2040-8978/17/8/085607.
URL http://stacks.iop.org/2040-8986/17/i=8/a=085607

[23] D. G. Bailey, Sub-pixel estimation of local extrema, in: Proceeding of Image and Vision Computing New Zealand, 2003, pp. 414–419.

[24] K. N. Ogle, Distortion of the image by prisms, J. Opt. Soc. Am. 41 (12) (1951) 1023–1028. doi:10.1364/JOSA.41.001023.
URL http://www.osapublishing.org/abstract.cfm?URI=josa-41-12-1023

[25] N. Yokoya, N. Miyamura, A. Iwasaki, Preprocessing of hyperspectral imagery with consideration of smile and keystone properties, in: Multispectral, Hyperspectral, and Ultraspectral Remote Sensing Technology, Techniques, and Applications III, Vol. 7857, 2010, p. 78570B. doi:10.1117/12.870437.

[26] X. Sun, B. L. Hu, L. B. Li, Z. H. Wang, An engineering prototype of Hadamard transform spectral imager based on Digital Micro-mirror Device, Optics and Laser Technology 44 (1) (2012) 210–217. doi:10.1016/j.optlastec.2011.06.020.

[27] DMD Optical Efficiency for Visible Wavelengths, Tech. Rep. DLPA083A, Texas Instruments Incorporated (05 2019).

[28] F. Viallefont-Robinet, D. Helder, R. Fraisse, A. Newbury, F. van den Bergh, D. Lee, S. Saunier, Comparison of mtf measurements using edge method: towards reference data set, Opt. Express 26 (26) (2018) 33625–33648. doi:10.1364/OE.26.033625.
URL http://www.opticsexpress.org/abstract.cfm?URI=oe-26-26-33625

Appendix A. Imaging

Appendix A.1. Distortion

We can asses the performance of the system as an imager, by turning all DMD mirrors to the 'on' position, obtaining the panchromatic image on the camera. A chrome on glass chequerboard target is placed in the focal plane of the system, and back-lit with a white light LED. The resultant image is shown in Figure 22. We don't observe significant distortion, and measurement of the size of the squares gives a magnification of 0.995. Due to the orientation of the DMD and the dimensions of the camera, the top right and bottom left corners of the image are cut off, although the majority of the camera is still available for use.

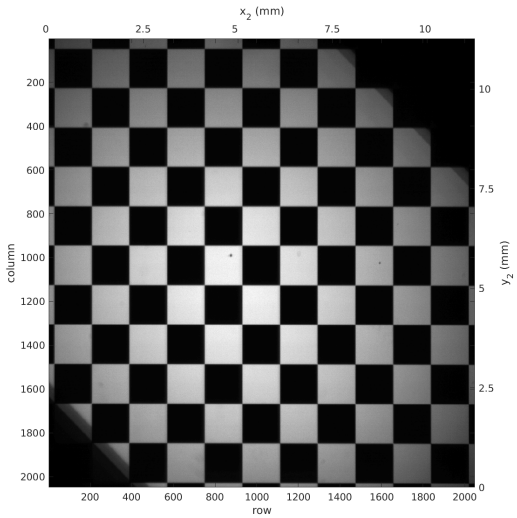

Figure 22: Panchromatic image with chrome on glass checkerboard target.

Appendix A.2. Modulation transfer function

The modulation transfer function (MTF) of the system was determined via the slanted edge method [28], with results shown in Figure 23. Given a pixel size of 5.5 μm, the system has a resolution of 11 μm (defined as the visibility of 21% at the half the Nyquist frequency).

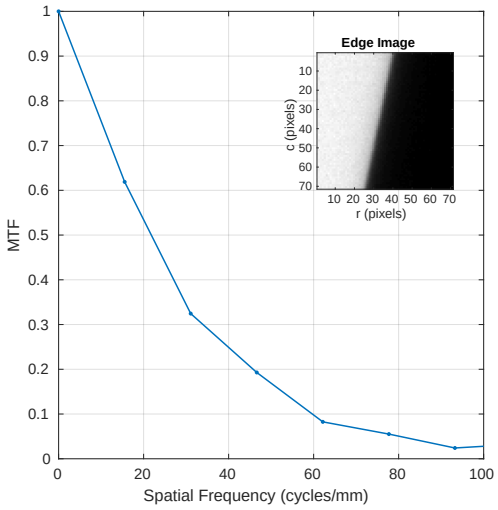

Figure 23: MTF of system calculated using the slanted edge method.

Appendix A.3. Wavelength Dependence of point spread function

As well as assessing the resolution of the system from scene to camera, it is key to consider the dispersed image of the scene formed onto the DMD. Indeed, this imaging is key in turning a spatial pattern on the DMD into a spatio-spectral filter prior to wavelength recombination and imaging on the camera. As the system is symmetric, one can consider either the imaging of the scene onto the DMD or equivalently the imaging of the DMD onto camera, the latter being more practical. We thus characterize the point spread function from the DMD to the camera, by opening a single mirror on the DMD and recording the corresponding image on the camera, for many different positions of the mirror across the DMD surface. Figures 24a and 24b show the collection of images on the camera when a single mirror is opened on the DMD at various positions. The scenes are illuminated by two different monochromatic wavelengths. We see that the point spread function (PSF) is small and does not change much with wavelength.

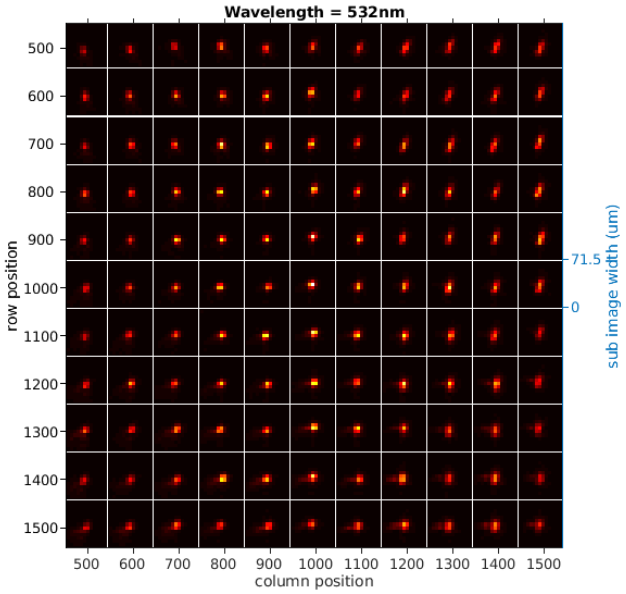

(a)

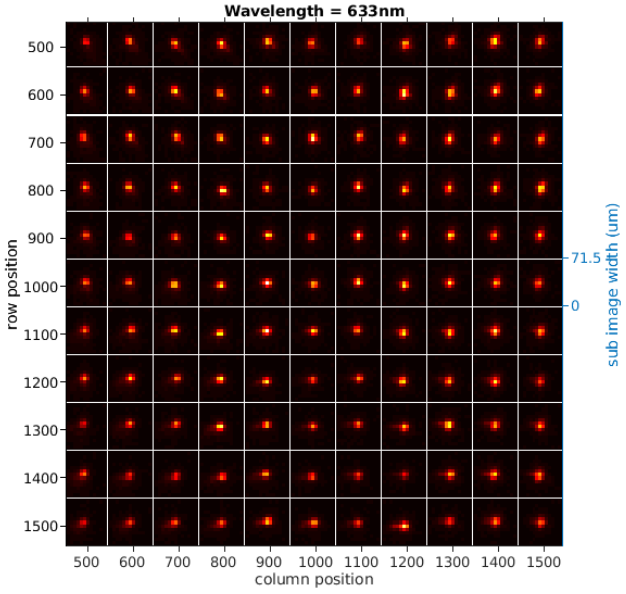

(b)

Figure 24: Subsection of camera image when a single mirror is opened on the DMD at different positions on the DMD surface, and the variation of this spot over the surface of the camera, at a) 532 nm and b) 633 nm.

Appendix B. Prism Distortion

Prism distortion occurs between the scene and the DMD planes and similarly between the DMD and the camera planes, both distortions compensating each other and resulting in the undistorted imaging described in the previous section. However, to determine the spatio-spectral filtering resulting from a particular DMD pattern, this distortion has to be properly calibrated. Distortion by the prism can be calculated by ray tracing in 3 dimensions. We consider that the initial facet of the prism lies in the (x, y) plane, as in Figure 25. Instead of using the usual spherical coordinates to describe the angle of the input beam to the facet, we use notation relating to the location on the scene and the optical axis (see Figure 4). The angle α depends on the horizontal coordinate on the scene, and is given by

$$\alpha = \alpha_c + \arctan\left(\frac{x_0}{F}\right) \tag{B.1}$$

where α_c is the angle of incidence for the optical axis at the central wavelength, as described in Section 3. Similarly, the angle β depends on the vertical coordinate, and in this case is zero for the optical axis.

$$\beta = \arctan\left(\frac{y_0}{F}\right) \tag{B.2}$$

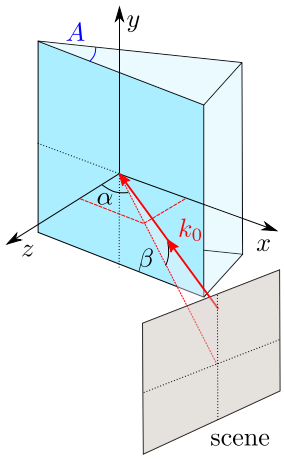

Figure 25: Schematic showing the angle conventions for the incident ray on the prism.

Using this notation, in the frame defined by the initial facet of the prism, the ray vector of the incoming light is given by

$$\boldsymbol{k_0} = \begin{bmatrix} k_{0x} \\ k_{0y} \\ k_{0z} \end{bmatrix} = k_0 \begin{bmatrix} u_{0x} \\ u_{0y} \\ u_{0z} \end{bmatrix} = k_0 \begin{bmatrix} \sin\alpha\cos\beta \\ \sin\beta \\ \cos\alpha\cos\beta \end{bmatrix} \tag{B.3}$$

To refract the beam through the first facet, it is simpler to reduce the problem to two dimensions by applying a rotation to the frame of reference around the z-axis. The ray vector $\boldsymbol{k_1}$ in the rotated frame can be written as :

$$\boldsymbol{k_1} = \boldsymbol{R_z}(\theta)\boldsymbol{k_0} \tag{B.4}$$

where the angle of rotation θ is such that the ray lies in a plane (x, z), i.e. $k_{1y} = 0$. The required angle of rotation is :

$$\theta = -\arctan\left(k_{0y}/k_{0x}\right) = -\arctan\left(u_{0y}/u_{0x}\right) \tag{B.5}$$

Inside the prism, refraction is calculated by Snell's law. The vector of the refracted ray is given by

$$\boldsymbol{k_2} = k_0 \begin{bmatrix} u_{1x} \\ 0 \\ \sqrt{n(\lambda)^2 - u_{1x}^2} \end{bmatrix} \tag{B.6}$$

The magnitude of this vector is now $n(\lambda)k_0$. Undoing the initial rotation gives the refracted k-vector in the original frame, or the vector of the beam of light inside the prism.

$$\boldsymbol{k_3} = \boldsymbol{R_z}(-\theta)\boldsymbol{k_2} \tag{B.7}$$

Now we consider the second facet, which lies at an angle A to the first facet, where A is the apex angle of the prism. We rotate this frame by $-A$ around the y axis so the exit facet now lies in the (y, x) plane.

$$\boldsymbol{k_4} = \boldsymbol{R_y}(-A)\boldsymbol{k_3} \tag{B.8}$$

Similarly to before, we wish to rotate this frame again so the beam inside the prism lies in the (x, z) plane. This requires a rotation about the z axis by angle $\phi = -\arctan(k_{4y}/k_{4x}) = -\arctan(u_{4y}/u_{4x})$:

$$\boldsymbol{k_5} = \boldsymbol{R_z}(\phi)\boldsymbol{k_4} \tag{B.9}$$

The k-vector k_5 is refracted once more upon exiting the prism:

$$\boldsymbol{k_6} = k_0 \begin{bmatrix} u_{5x} \\ 0 \\ \sqrt{1 - u_{5x}^2} \end{bmatrix} \tag{B.10}$$

This vector has magnitude k_0. Finally, undoing the two previous rotations (in the correct order) gives the vector of the final ray exiting the prism.

$$\boldsymbol{k_{out}} = \boldsymbol{R_y}(A)\boldsymbol{R_z}(-\phi)\boldsymbol{k_5} \tag{B.11}$$

The angle between $\boldsymbol{k_{out}}$ and $\boldsymbol{k_0}$ is the angle of deviation, which varies as function of β, giving rise to smile distortion. For our system dimensions, the maximum $\beta_{max} = 1.61°$, so the field of view is narrow enough that small angle

approximations can be used, leading to a quadratic relationship between the change in the horizontal location of the incident light x_i dependent on its vertical location y_i.

$$\Delta x_i \approx S y_i^2 \tag{B.12}$$

For our system we have $S = 1.2042/\text{m}$ at wavelength 550 nm.

The smile distortion is calculated and shown in Figure 26 for wavelengths 400 and 700 nm, compared to experimentally measured data. It's clear that the smile distortion in this case is negligibly dependent on the wavelength. These equations can also be used to determine the extent of keystone distortion if necessary.

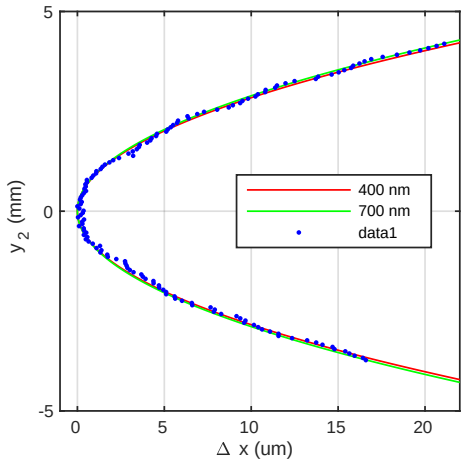

Figure 26: Smile distortion model for an arbitrary DMD slit position at wavelengths 400 and 700 nm, compared to experimentally measured data at 611 nm.